Version of Record: https://www.sciencedirect.com/science/article/pii/S209549561831235X
Manuscript_5c979e8e676f7e028568549a394fec21

Effect of cation (Li^+, Na^+, K^+, Rb^+, Cs^+) in aqueous electrolyte on the electrochemical redox of Prussian Blue Analogue (PBA) cathodes

Satyajit Phadke[a], Roman Mysyk [b], Mérièm Anouti[a,*]

[a] *Université de Tours, Laboratoire PCM2E, Bâtiment J, Parc de Grandmont, 37200 Tours, France*
[b] *Parque Tecnologico C/Albert Einstein 48 CP 01510 Milano (Alava), Spain*

Abstract

Prussian blue analogue (PBA) material is a promising cathode for applications in Na-ion and K-ion batteries which can support high c-rates for charge and discharge. In this study, the material of composition $[K_2Cu^{II}Fe^{II}(CN)_6]$ was synthesized and its structural and electrochemical redox behaviour was investigated with 5 different alkali insertion cations (Li^+, Na^+, K^+, Rb^+, Cs^+). Galvanostatic measurements indicate that the redox potential strongly depends on the ionic radius of the inserted cation. The redox potential varies by ~ 400 mV between using Li^+ (0.79 Å) or Cs^+ (1.73 Å) in the electrolyte. The underlying modification of the Fe^{2+}/Fe^{3+} redox potential in PBA is proposed to be due to the weakening of the Fe–C bond in the material. This hypothesis is supported by XRD measurements which reveal that the lattice parameter of the de-intercalated host structure follows the same trend of monotonic increase with the cation size. The relatively minor volume changes accompanying the redox (1.2%–2.4%) allow the PBA to accommodate differently sized cations, although the structural hindrances are quite pronounced at high c-rates for the larger ones (Rb^+ and Cs^+). Cycle aging studies indicate that the minimum capacity fade rate is observed in case of K^+ and Rb^+ containing electrolyte. The peak intensity corresponding to the [220] crystallographic plane varies depending on the state of charge of PBA, since this plane contains the insertion cations. Owing to the sensitivity of the redox potential to the insertion cation coupled with the observed fast ion-exchange ability, the PBA material may find additional analytical applications such as ion sensing or filtration devices.

Keywords Prussian blue; Cathode; Alkali cations; XRD; Batteries

Corresponding author.

Email address: meriem.anouti@univ-tours.fr (M. Anouti).

Telephone +33247366951

1. Introduction

Energy storage devices are gaining global importance owing to their increasing use in portable electronic devices, electric vehicles and stationary storage applications [1]. Additional high power capability (W kg^{-1}) is desirable for specific cases such as acceleration and regenerative braking in electric vehicles, elevator backup systems and power reliability systems for aviation [2]. Traditionally, Li-ion batteries containing intercalation cathodes such as $LiCoO_2$ (LCO), $LiNi_{0.33}Mn_{0.33}Co_{0.33}O_2$ (NMC) or $LiFePO_4$ (LFP) possess high energy density (120–180 Wh kg^{-1}) but lack in terms of power density (W kg^{-1}) [3,4]. Due to the diffusion limitations during intercalation and de-intercalation of Li^+, the obtained capacity (mAh g^{-1}) and nominal voltage (V) for these materials tends to reduce drastically at high c-rates.

Most of the intercalation electrode materials are also very cation specific. By contrast, Prussian blue analogue (PBA) materials with the chemical formula $[A_xM'_aM''_b(CN)_6]$ have been shown to reversibly intercalate a wide variety of cations [5–7]. Although, the theoretical gravimetric specific capacity is a little low for use as battery electrodes (60–100 mAh g^{-1}), owing to their fast intercalation kinetics which are suitable for used as electrodes in hybrid supercapacitors [8–10]. The PBA materials have been shown to retain a large fraction of their theoretical capacity at scan rates as high as 50 C [9–12]. Other pseudocapacitive electrode materials in this category include inorganic materials such as MnO_2, V_2O_5 [13–17] and organic materials such as PAQS, PPy, Polyaniline [18–22].

PBAs are members of a family of multifunctional molecular materials with electronically active metal sublattices known for their unusual electronic, optical, photothermal and magnetic properties [23–26]. Margadonna et al. reported using synchrotron X-ray diffraction measurements that the PBA exhibits isotropic near zero thermal expansion (ZTE) in a large temperature range between 4.2 and 300 K [27]. Their high compositional flexibility combined with a host of interesting physical properties could be exploited to design multifunctional energy storage materials through the suitable selection of transition metal ions and/or interstitial units.

Recently there have been reports on the use of this material as a cathode in Na, K and Li-ion in batteries and capacitors [28–31]. However, to the best of our knowledge, an integrated structure-redox behavior study using different cations has not been reported. In this study, we investigate the effect of inserted cation (Li^+, Na^+, K^+, Rb^+, Cs^+) on the obtained capacity (mAh g^{-1}), redox potential (V) and capacity fade rate (%/cycle) of the synthesized PBA material. The observed structural variations of the PBA host material from XRD measurements are used to explain the contrasting electrochemical behavior obtained in the presence of different cations.

2.Experimental

2.1. Material synthesis

Prussian blue analogue material with the following composition $K_2Cu^{II}Fe^{II}(CN)_6$ was prepared by mixing equal volumes of 50 mM aqueous solution of $K_4Fe(CN)_6$ and 100 mM

aqueous solution of $Cu(NO_3)_2$. The two solutions (120 mL each) were added dropwise to 60 mL of de-ionized water in a beaker. The de-ionized water was kept under magnetic stirring during the addition. The reaction between the two chemicals is fast and the PBA material instantaneously precipitates out. The precipitate was removed by vacuum filtration using Whatmann filter paper (GF/A). Following this, the precipitate was washed several times with water and then dried at 60 °C for 10 h. The as-synthesized powder is in the reduced (that is the discharged) state.

2.2. Electrode preparation

For preparing the electrodes, the PBA powder was dry and then mixed with Ketjen Black (KB) in a mortar and pestle. The powder mixture was added to a solution of N-methyl pyrrolidone (NMP) containing 5 wt% Polyvinylidene fluoride (PVDF). The final electrode composition was PBA:KB:PVDF (80:10:10) by weight. The obtained slurry was coated on graphite paper (Sigracet BC, SGL Carbon) and dried at 90 °C under vacuum for 3 h to remove the NMP.

2.3. Electrolytes

The electrolytes were prepared by dissolving the nitrates of the respective alkali cations (Li^+, Na^+, K^+, Rb^+, Cs^+) in de-ionized water to obtain a 1 M concentration. Using the same anion (nitrate) ensures that the only difference between the electrolytes is the cation. The pH of the electrolyte was adjusted to 2 by addition of nitric acid.

2.4.Electrochemical testing

For electrochemical testing, standard three electrode cells were assembled. The counter electrode was a commercial AC electrode while a standard Ag/AgCl reference electrode was used. The electrodes were immersed in a beaker containing the appropriate electrolyte. The electrochemical measurements were performed on a VMP-3 Biologic Potentiostat. The cycled electrodes were stopped, either in the charged state or the discharged state, removed from the electrolyte and washed thoroughly with water prior to XRD characterization.

2.5.XRD characterization

After drying, the as-prepared and charged and discharged electrodes were subjected to XRD under the following conditions. The wavelength of the Cu K_α radiation was λ = 1.5418 Å, while the angular resolution in 2θ scans was 0.02° over range of 10°–70°. Structural refinement of the obtained data was done using PowderCell software. Crystal structure visualizations were prepared using VESTA software.

3.Results and discussion

The crystal structure of the as-synthesized material has the formula $K_2Cu^{II}Fe^{II}(CN)_6$ and belongs to the cubic space group $Fm\bar{3}m$. The dimension of the unit cell as calculated from XRD measurements on the PBA is a_0 = 9.9954 Å. Each unit cell contains 4 formula units of the molecule. The Fe^{2+} ions occupy the corners and face centered positions of the unit cell as shown in Fig. 1. A C≡N group (not shown) is located between neighboring Cu and Fe ions to

form the network of the host structure. The C≡N group is oriented in a way to form Fe–C and Cu–N bonds as shown in Fig. 1. In each unit cell, the eight K^+ cations occupy the Wyckoff position 8c. Out of these 8 cations, only 4 K^+ ions can be reversibly intercalated during the electrochemical reduction corresponding to the four Fe^{2+}/Fe^{3+} redox centers as shown in reactions (1) and (2). During oxidation, the Fe^{2+} is re-oxidized to Fe^{3+} and de-intercalation of the itinerant cation occurs as represented in Fig. 1. The calculated theoretical discharge capacity based on this reaction is 63 mAh g^{-1}. The obtained positions of the ions by refinement of the XRD data of the as-synthesized material are shown in Table 1.

Fig 1. Crystal structure of $K_2CuFe(CN)_6$ in the discharged (intercalated) and the charged (de-intercalated) state. K^+ ions are shown in red and C≡N bonds are not shown for clarity. Fe and Cu lattice positions are labelled accordingly.

Table 1. Crystal structure data for $K_2CuFe(CN)_6$.

Atom	Site	*x*	*y*	*z*	B_{iso}	SOF
Fe	4a	0.0000	0.0000	0.0000	3.5900	1.0000
Cu	4b	0.5000	0.5000	0.5000	1.3600	1.0000
K	8c	0.2500	0.2500	0.2500	17.0400	1.0000
C	24e	0.7948	0.0000	0.0000	4.7900	1.0000
N	24e	0.6860	0.0000	0.0000	3.1400	1.0000

Space group ($Fm\bar{3}m$, a_0 = 9.9954 Å).

The five cations chosen for this investigation are Li^+, Na^+, K^+, Rb^+ and Cs^+. The radii of the ions as well as their diffusion coefficients obtained from the literature are shown in Table 2 [32,33]. It can be seen that the ionic radius of Li^+ is almost half of K^+, while that of Cs^+ is approximately 30% higher.

Table 2. Ionic radii of cations of interest (A = Li^+, Na^+, K^+, Rb^+ and Cs^+) in aqueous solutions, along with their diffusivity (25 °C) in aqueous electrolytes [32,33].

Ion type	Solvation-radius (Å)	Diffusivity (10^{-10} m^2 s^{-1}) at 25 °C
Li^+	0.79	11.80
Na^+	1.07	12.20
K^+	1.38	20.02
Rb^+	1.64	21.10 [34]
Cs^+	1.73	20.00 [34]

3.1. Electrochemical measurements

3.1.1. Redox potentials

The cyclic voltammetry at 1 mV s^{-1} performed on the PBA electrodes in electrolytes containing different cations is shown in Fig. 2(a). Based on the large variation in the shape the CVs and the redox potentials, it is obvious that the nature of inserted cation has a significant impact on the electronic environment of the Fe^{2+}/Fe^{3+} redox center. In case of Li^+, a broad profile consisting of a multiple peaks is observed over a wide potential range of ~800 mV. In case of Na^+, two distinct peaks can be observed during charge and discharge. By

contrast, it is found that, for the larger cations (Rb^+ and Cs^+), there is only a single redox peak.

Table 3. Redox potentials (V vs. SHE) obtained from the oxidation and reduction peaks observed during cyclic voltammetry (1 mV s^{-1}) of PBA.

Cation	E_{PA} (V)	E_{PC} (V)	$E_{1/2}$ (V vs. SHE)
Li^+	0.92, 0.74, 0.52, 0.22	0.87, 0.57, 0.29, 0.13	0.58
Na^+	0.90, 0.65	0.82, 0.55	0.60
K^+	0.79	0.52	0.66
Rb^+	0.94	0.76	0.85
Cs^+	1.04	0.87	0.95

Reduction (E_{PC}) and oxidation (E_{PA}) peak potentials. $E_{1/2}$ is the half wave potential for redox of the most prominent peaks.

The reduction and oxidation peak potentials observed from cyclic voltammetry are summarized in Table 3. The redox potential is estimated by taking the average of a pair of the prominent oxidation and reduction peaks. It can be seen that the average redox potential increases with increasing cation size and is the highest for Cs^+ cation (0.95 V). By simply exchanging the cation in the electrolyte from Li^+ to Cs^+, the redox potential shifts by almost ~400 mV. In fact, the cation dependence of redox potential has been reported previously by two groups separately working on Prussian Blue thin film electrodes of composition $KFe^{II}Fe^{III}(CN)_6$ in the 1980s [7,35]. However, no explanation was offered for the observation. Since we observe the same effect, in a material of different composition $K_2Cu^{II}Fe^{II}(CN)_6$, it appears that this is generally applicable to materials of hexametallocyanate family.

When the CV is conducted at a lower scan rate (0.1 mV s^{-1}), the obtained scans are significantly modified as shown in Fig. 2(b). For all cations, there is an increase in electrochemical reversibility as observed from the lowering of ($E_{PA} - E_{PC}$). In case of Rb^+ and Cs^+, the peaks appear distinctly sharper indicating that diffusion of these cations in the PBA is more sluggish as compared to Na^+ and K^+. As a result, allowing more time for the diffusion of cations by lowering the scan rate significantly influences the electrochemical behavior.

Fig. 2 Cyclic voltammetry at (a) 1 mV s^{-1} and (b) 0.1 mV s^{-1} on PBA under different itinerant cations

In a previous work of Goodenough, it was shown that the potential of the Fe^{2+}/Fe^{3+} redox center can shift significantly based on the surrounding environment. In such materials the redox potential was found to shift by ~800 mV depending on the choice of the polyanions

$(SO_4)^{2-}$, $(PO_4)^{3-}$, $(SiO_4)^{4-}$, $(AsO_4)^{3-}$ or $(WO_4)^{3-}$ [36]. It was shown that, as the Fe–O bond length increases, the Fe^{2+}/Fe^{3+} redox potential also increases [37,38]. More recently, it was predicted that by analogy in PBA materials where each Fe is bonded to 6 carbons, it is the nature of this Fe–C bond which would primarily affect the redox potential [39]. Based on the redox potentials obtained in this work, it appears that the Fe–C bond should be the longest in the material when Cs^+ cation is used. This in turn would translate to the increase of the redox potential as observed. By contrast, in case of Li^+ ion insertion, the redox potential observed is the lowest (0.58 V), which would imply that the Fe–C bond is the shortest. This hypothesis is supported by the XRD results which are discussed in a following section.

3.1.2.Voltage profiles and reversible capacity

The potential profiles obtained from galvanostatic cycling in presence of different cations (Li^+, K^+, Rb^+ and Cs^+) are shown in Fig. 3(a-d). It can be seen that irrespective of the cation in the electrolyte, the capacity on the first charge (1 C) is ~60 mAh g^{-1} and close to the theoretical capacity. However, during the first discharge, the capacity is lower and highly dependent on the cation. The extent of unrecovered capacity (shown in green) is larger for the larger cations namely Rb^+ (11 mAh g^{-1}) and Cs^+ (24.4 mAh g^{-1}). Additionally, the reduction in capacity (shown in red) by going to a higher c-rate (5 C) is also highest for these cations. This is indicative of diffusion constraints for the larger cations as inferred from the cyclic voltammetry.

The other distinction between cations is the flatness of the potential profiles. A flat profile during electrochemical reaction is observed when a two-phase system is encountered such as that occurring in case of $LiFePO_4$ or $Li_4Ti_5O_{12}$ [38,40,41]. In case of Li-Bi batteries also, a varying voltage is observed in the single phase region whereas a flat voltage when the cathode enters the two-phase region [42]. It is possible that the insertion of the larger cations (Rb^+ and Cs^+) causes significant structural distortion leading to a similar effect. On the other hand, the insertion of small cations such as Li^+ is easier to accommodate into the structure. The voltage profiles of Na^+ and K^+ exhibit intermediate behaviour; where during the initial portion (< 20%) of the discharge the voltage changes continuously whereas during the remaining part, the voltage remains relatively flat. These two regions are labelled (separated by a dotted line) in Fig. 3(b) taking K^+ as an example.

Fig. 3 Charge and discharge potential profile for the first cycle at 1 C and 5 C in electrolytes with different cations (a) Li^+, (b) K^+, (c) Rb^+ and (d) Cs^+. The reduction in discharge capacity (mAh g^{-1}) upon increasing the current from 1 C to 5 C is shown in red. The unrecoverable capacity of the first charge at 1 C is labelled in green.

3.1.3.Capacity retention

The discharge capacity obtained for various itinerant cations at 5 C for the first 50 cycles is compared in Fig. 4. The charge and discharge voltage limits for the galvanostatic cycling were selected based on the cyclic voltammetry results shown earlier to ensure completion of the redox reaction. In Fig. 4(a), the actual capacities are plotted as a function of the cycle number, whereas the normalized values are shown in Fig. 4(b).

Fig. 4 Discharge capacity expressed in mAh g^{-1} (a) and normalized discharge capacity (b) as functions of the cycle number for PBA under galvanostatic cycling (5 C) with different itinerant cations

It can be seen that the initial capacity obtained in case of Na^+ (56.6 mAh g^{-1}) and K^+ (55.1 mAh g^{-1}) is the highest and close to the theoretical capacity. The initial capacities and the capacity fade rate (%/cycle) calculated by linear fitting of the data are summarized in Table 4. For Li^+, although the initial capacity is quite close to that of Na^+ and K^+, the capacity fade rate was significantly higher than for all other cations (0.76 %/cycle). This is partly explained by the higher solubility of the PBA (Li^+ ion intercalated). In case of Li^+, the electrolyte assumed the characteristic yellow color of ferrocyanide ion ($Fe(CN)_6^{4-}$) after a few cycles indicating loss of material from the electrode. In case of all other cations, the electrolyte remained transparent until the completion of the test. For other cations such as Rb^+ and Cs^+, although the capacity obtained is much lower, the capacity fade rates are still quite low (0.09 and 0.26 %/cycle respectively).

By comparing the discharge capacity obtained at 1 C and 5 C for all cations (Table 4), it is clear that the larger cations such as Rb^+ and especially Cs^+ face structural hindrances due to their large ionic radius. This becomes more evident at the higher c-rate, where Rb^+ (41 mAh g^{-1}) and Cs^+ (28 mAh g^{-1}) exhibit much lower capacity. The channel radius in the PBA lattice is approximately 1.6 Å, which is smaller than the ionic radius of Rb^+ (1.64 Å) and Cs^+ (1.73 Å) [6]. Other cations which are much smaller exhibit a very small (<4%) decrease in capacity on increasing the c-rate from 1 C to 5 C.

3.2.XRD measurements

To understand the accompanying structural changes, XRD measurements were conducted on the electrodes while in the fully charged (oxidized state), fully discharged (reduced state) and on the pristine material (Fig 5). The obtained XRD spectra clearly demonstrate three peaks belonging to the carbon current collector which are invariant (Fig 5a). These are indicated by gray dotted lines in Fig. 5(b). The remaining peaks belong to the active material in the electrode and are similar to those reported in literature [43–45]. These have been indexed accordingly.

Fig. 5 (a) Obtained XRD patterns for pristine PBA (blue), PBA in the charged/de-intercalated state (green) and the discharged/intercalated state (red). Pattern for uncoated carbon current collector is also shown (black). (b) Calculated unit cell parameters from the XRD measurements as a function of the insertion cation for the PBA material in the intercalated state (red) and the de-intercalated state (green). Also shown are the respective measured redox potentials

Table 4. Initial discharge capacity (mAh g^{-1}) obtained while using different itinerant cations at 5 C and 1 C rate of galvanostatic cycling along with calculated capacity fade rate (%/cycle).

Cation inserted	Initial capacity (mAh g^{-1}) at 5 C	Initial capacity (mAh g^{-1}) at 1 C	Capacity fade (%/cycle)
Li^+	51.36	54.84	0.76
Na^+	56.80	58.90	0.16
K^+	55.15	57.76	0.06
Rb^+	41.44	51.74	0.09
Cs^+	28.30	37.11	0.26

3.3.Cation nature and respiration of unit cell

As seen in Fig. 6, the peaks corresponding to PBA, shift towards higher 2θ upon discharge indicating that the unit cell contracts upon intercalation of ions. This observation was found to apply to insertion of all cations studied irrespective of their size. The structural contraction has been observed previously in other materials of the hexacyanometallate family [43].

The calculated unit cell dimensions for PBA under cycling with different cations are shown in Fig. 5(b) for the discharged and charged state respectively. It can be seen that in the charged (or de-intercalated) state, there is a strong dependence of the unit cell dimension and the choice of the itinerant cation. In case of using Cs^+ as the itinerant cation, the dimension is the largest (10.0697 Å) whereas in case of Li^+, it is the smallest (10.0121 Å). According to the Equations (1) and (2) shown earlier, the composition of the material in the de-intercalated state should be the identical [$KCu^{II}Fe^{III}(CN)_6$] irrespective of the cation employed for the redox reaction. However, it is clear from the obtained XRD data that the PBA host material undergoes compositional changes resulting in an expansion of the unit cell.

One of the possibilities is cation exchange between the electrolyte and electrode as shown in the schematic and reaction in Fig. 7. Since the PBA electrodes are maintained in the electrolyte containing a large excess (~1000 times) of a particular cation, it is possible that exchange occurs between K^+ ions in the structure and the A^+ ions in the electrolyte. As a result, the modified composition would be closer to $ACu^{II}Fe^{III}(CN)_6$ where A = Li^+, Na^+, K^+, Rb^+ or Cs^+. This would explain the direct relationship between unit cell dimension and the ionic radius of the cation. Indeed, Prussian blue is known to be zeolitic in nature with the ability to readily exchange group I cations in aqueous solutions [6,46–48]. This cation-exchange ability is aided by the relatively small $\%\Delta V$ during cycling which ranges between 2.42% and 1.13% in case of Cs^+ and Li^+ as shown in Fig. 5(b). These are quite small in comparison to those observed other cathode materials such as $LiFePO_4$ (6.81%) [38].

As a consequence, it can be seen that the PBA host material is not only exceptionally flexible to cation size but can also accommodate quite high c-rates with ease. For example the discharge capacity in case of Li^+, Na^+ and K^+ ion only reduces by ~4% on increasing the current from 1 C to 5 C. The average dimension of the cubic particles of PBA is ~40 nm (400 Å) which provides a large electrode/electrolyte interface. Owing to the cubic crystal symmetry (6 faces of the cube can be used for cation exchange) the estimated diffusion distance would only be ~20 unit cells.

In the discharged state (intercalated) the PBA material lattice dimension does not exhibit any specific trend based on the cation size. The unit cell dimensions are mostly centered around the pristine material.

The two most prominent peaks in the XRD pattern correspond to the [200] and [220] crystallographic planes. A close up view of these peaks is shown in Fig. 6(a) for the charged and the discharged electrodes. The orientation of these planes in the unit cell and the atoms positioned on the planes are shown in Fig. 6(b). It can be seen that the insertion cation is located on the [220] plane but not on the [200] plane. Due to this we can clearly observe an increase in the intensity of the peak corresponding to [220] with the progression of discharge (intercalation). The peak height of the [200] plane is invariant. The graph shown here is that for K^+ but the same phenomenon was observed for all cations.

Fig. 6 (a) Superimposed XRD pattern of PBA in the intercalated (discharged) and de-intercalated (charged) state. Itinerant cation is K^+. (b) Crystallographic planes [220] and [200] corresponding to two prominent peaks observed in the powder XRD pattern.

3.4.Structural interpretation of electrochemical redox potential

It can be seen that the increasing trend of the potential matches well with the increasing cation size (Fig. 7a-c) as well as the increasing lattice parameters in the charged state. This correlation further extends even to non-alkali cations as we found in case of ammonium ion during galvanostatic cycling. As shown in Fig. 7(b), the redox potential obtained (0.93 V vs. SHE) is slight lower compared to Cs^+ (0.95 V) in Fig. 3(d). The ionic radius of NH_4^+ (1.54 Å) is also slightly lower than that of Cs^+ (1.73 Å) [33,47]. The observed cation ionic radius dependent expansion of the PBA host framework implies a larger stretching (and more weakening) of the Fe–C bond for a larger insertion cation.

Fig. 7 Galvanostatic charge discharge curve for PBA with (a) Li^+ and (b) NH_4^+ and (c) Na^+ itinerant cation at 1C rate. Cations are inserted during discharge and vice versa as indicated

This agrees well with the hypothesis presented in a previous section, wherein the Fe–C bond was predicted to be the largest for the case of Cs^+ and smallest for the case of Li^+ based on the measured redox potential. The cation present in the electrolyte is solely responsible for the variation in the redox potential of the host framework since the starting electrode material is the same in all cases. This also implies that the cation exchange process occurs (Fig. 8) quite rapidly in these materials and as soon as they are placed in contact with the electrolyte. In the galvanostatic experiments presented, the electrodes were placed in the electrolyte only few minutes prior to the start of cycling. However, in all cases the redox potentials were already modified starting from the first half cycle of the testing. Owing to the large dependence of the redox potential on the electrolyte cation and fast response time, this material may also find use in ion-sensing and filtration applications in addition to energy storage devices.

Fig. 8 Sub-section of the PBA unit cell showing the arrangement of Fe, Cu, C and N atoms around the itinerant cation. Dominant cation in the electrolyte (grey) depends on the electrolyte composition and could be Li^+, Na^+, K^+, Rb^+, Cs^+ which may be freely exchanged with the K^+ cation present in the as-synthesized material.

4.Conclusions

In this study, the intercalation behaviour of different cations into the PBA host cathode material is investigated. Although PBA can reversibly intercalate all tested alkali cations, the capacities obtained at 1 C and 5 C are dependent on the size of the cation and seem to be independent of the cation diffusivity in the electrolyte. Galvanostatic and cyclic voltammetry measurements indicate that the structural hindrance to diffusion of larger cations (Rb^+ and Cs^+) within the PBA structure results in a lower capacity. Based on aging studies it was found that K^+ and Na^+ are ideally suited for this cathode from a capacity perspective (>55 mAh g^{-1} at 5 C), whereas K^+ and Rb^+ cations exhibit the best capacity retention of 0.06 %/cycle and 0.09 %/cycle respectively. The redox potential was found to be strongly dependent on the size of the insertion cation. Structural investigations using XRD measurements indicate that the expansion of the unit cell and resulting lengthening of the Fe–C bond can explain the increase of the redox potential with cation size. The intensity of the peak corresponding to the plane [220] which contains the itinerant cation was found to be sensitive to the state of charge of the cathode. The sensitivity of the redox potential to the insertion cation coupled with the fast ion-exchange ability, renders the PBA material suitable for ion sensing device applications in addition to energy storage devices. Further work is required to better understand the role of the solvent in the intercalation mechanism.

Conflicts of interest

There are no conflicts to declare.

Acknowledgments

The authors would like to thank “Le Studium Loire Valley Institute for Advanced Studies” for financial and logistical support to the researchers involved in this study and “Region Centre” for financial support under the “Lavoisier” program.

References

[1] E. Karden, S. Ploumen, B. Fricke, T. Miller, K. Snyder. J. Power Sources. 168(1)(2007)2-11.
[2] J. Cao, A. Emadi. IEEE Trans. Power Electron. 27(1)(2012)122-132.
[3] M. Xu, L. Fei, W. Zhang, T. Li, W. Lu, N. Zhang, Y. Lai, Z. Zhang, J. Fang, K. Zhang, J. Li, H. Huang. Nano Lett. 17(3)(2017)1670-1677.
[4] J. B. Goodenough, K.-S. Park. J. Am. Chem. Soc., 135(4)(2013)1167-1176.
[5] K. Itaya, T. Ataka, S. Toshima. J. Am. Chem. Soc., 104(18)(1982)4767-4772.
[6] K. Itaya, I. Uchida, V. D. Neff. Acc. Chem. Res. 19(6)(1986)162-168.

[7] C. A. Lundgren, R. W. Murray. Inorg. Chem. 27(5)(1988)933-939.
[8] A. Eftekhari. J. Power Sources. 126(1)(2004)221-228.
[9] A. J. Fernández-Ropero, M. J. Piernas-Muñoz, E. Castillo-Martínez, T. Rojo, M. Casas-Cabanas. Electrochim. Acta 210(2016)352-357.
[10] X.-y. Wu, M.-y. Sun, Y.-f. Shen, J.-f. Qian, Y.-l. Cao, X.-p. Ai, H.-x. Yang. ChemSusChem 7(2)(2014)407-411.
[11] L. Wang, Y. Lu, J. Liu, M. Xu, J. Cheng, D. Zhang, J. B. Goodenough. Angew. Chem. Int. Ed. 52(7)(2013)1964-1967.
[12] L. Wang, J. Song, R. Qiao, L. A. Wray, M. A. Hossain, Y.-D. Chuang, W. Yang, Y. Lu, D. Evans, J.-J. Lee, S. Vail, X. Zhao, M. Nishijima, S. Kakimoto, J. B. Goodenough. J. Am. Chem. Soc., 137(7)(2015)2548-2554.
[13] A. Boisset, L. Athouël, J. Jacquemin, P. Porion, T. Brousse, M. Anouti. J. Phys. Chem. C 117(15)(2013)7408-7422.
[14] C. Y. Foo, A. Sumboja, D. J. H. Tan, J. Wang, P. S. Lee. Adv. Energy. Mater 4(12)(2014)1400236.
[15] X. Lu, M. Yu, G. Wang, T. Zhai, S. Xie, Y. Ling, Y. Tong, Y. Li. Adv. Mater. 25(2)(2013)267-272.
[16] G. Wee, H. Z. Soh, Y. L. Cheah, S. G. Mhaisalkar, M. Srinivasan. J. Mater. Chem. 20(32)(2010)6720-6725.
[17] W.-y. Zou, W. Wang, B.-l. He, M.-l. Sun, Y.-s. Yin. J. Power Sources. 195(21)(2010)7489-7493.
[18] Y.-H. Huang, J. B. Goodenough. Chem. Mater 20(23)(2008)7237-7241.
[19] W. Lee, S. Suzuki, M. Miyayama. Nanomaterials 4(3)(2014).
[20] S. Phadke, M. Cao, M. Anouti. ChemSusChem 11(5)(2018)965-974.
[21] S. Zhou, H. Zhang, Q. Zhao, X. Wang, J. Li, F. Wang. Carbon 52(2013)440-450.
[22] Y. Zhou, B. Wang, C. Liu, N. Han, X. Xu, F. Zhao, J. Fan, Y. Li. Nano Energy 15(2015)654-661.
[23] S. Ferlay, T. Mallah, R. Ouahès, P. Veillet, M. Verdaguer. Nature 378(1995)701.
[24] G. Fu, W. Liu, Y. Li, Y. Jin, L. Jiang, X. Liang, S. Feng, Z. Dai. Bioconjug Chem. 25(9)(2014)1655-1663.
[25] A. Goujon, O. Roubeau, F. Varret, A. Dolbecq, A. Bleuzen, M. Verdaguer. Eur. Phys. J. B 14(1)(2000)115-124.
[26] A. Widmann, H. Kahlert, I. Petrovic-Prelevic, H. Wulff, J. V. Yakhmi, N. Bagkar, F. Scholz. Inorg Chem. 41(22)(2002)5706-5715.
[27] S. Margadonna, K. Prassides, A. N. Fitch. J. Am. Chem. Soc.,126(47)(2004)15390-15391.
[28] F. Wang, X. Wu, C. Li, Y. Zhu, L. Fu, Y. Wu, X. Liu. Energy Environ. Sci. 9(12)(2016)3570-3611.
[29] Z. Xing, S. Wang, A. Yu, Z. Chen. Nano Energy 50(2018)229-244.
[30] D. Zhang, J. Zhang, Z. Yang, X. Ren, H. Mao, X. Yang, J. Yang, Y. Qian. Chem. Commun. 53(76)(2017)10556-10559.
[31] L. Zhou, M. Zhang, Y. Wang, Y. Zhu, L. Fu, X. Liu, Y. Wu, W. Huang. Electrochim. Acta 232(2017)106-113.
[32] J. Mähler, I. Persson. Inorg. Chem.51(1)(2012)425-438.
[33] R. Shannon. A Acta Crystallogr. A 32(5)(1976)751-767.
[34] S. H. Lee, J. C. Rasaiah. J. Phys. Chem. 100(4)(1996)1420-1425.
[35] S. Sinha, B. D. Humphrey, A. B. Bocarsly. Inorg. Chem.23(2)(1984)203-212.
[36] A. Manthiram, J. B. Goodenough. J. Power Sources. 26(3)(1989)403-408.
[37] C. Sirisopanaporn, C. Masquelier, P. G. Bruce, A. R. Armstrong, R. Dominko. J. Am. Chem. Soc., 133(5)(2011)1263-1265.
[38] A. K. Padhi, K. S. Nanjundaswamy, J. B. Goodenough. J. Electrochem. Soc. 144(4)(1997)1188-1194.
[39] Y. Lu, L. Wang, J. Cheng, J. B. Goodenough. Chem. Commun. 48(52)(2012)6544-6546.
[40] M. Kitta, T. Akita, S. Tanaka, M. Kohyama. J. Power Sources. 257(2014)120-125.
[41] M. Kitta, M. Kohyama. Phys. Chem. Chem. Phys. 19(18)(2017)11581-11587.
[42] X. Ning, S. Phadke, B. Chung, H. Yin, P. Burke, D. R. Sadoway. J. Power Sources. 275(2015)370-376.
[43] T. Gupta, A. Kim, S. Phadke, S. Biswas, T. Luong, B. J. Hertzberg, M. Chamoun, K. Evans-Lutterodt, D. A. Steingart. J. Power Sources. 305(2016)22-29.
[44] D. O. Ojwang, J. Grins, D. Wardecki, M. Valvo, V. Renman, L. Häggström, T. Ericsson, T. Gustafsson, A. Mahmoud, R. P. Hermann, G. Svensson. Inorg. Chem.55(12)(2016)5924-5934.
[45] C. D. Wessells, R. A. Huggins, Y. Cui. Nat. Commun. 2(2011)550.
[46] A. Dostal, G. Kauschka, S. J. Reddy, F. Scholz. J. Electroanal. Chem. 406(1)(1996)155-163.
[47] V. Sidey. Acta Cryst. B 72(4)(2016)626-633.
[48] S. Zamponi, M. Berrettoni, P. J. Kulesza, K. Miecznikowski, M. A. Malik, O. Makowski, R. Marassi. Electrochim. Acta 48(28)(2003)4261-4269.

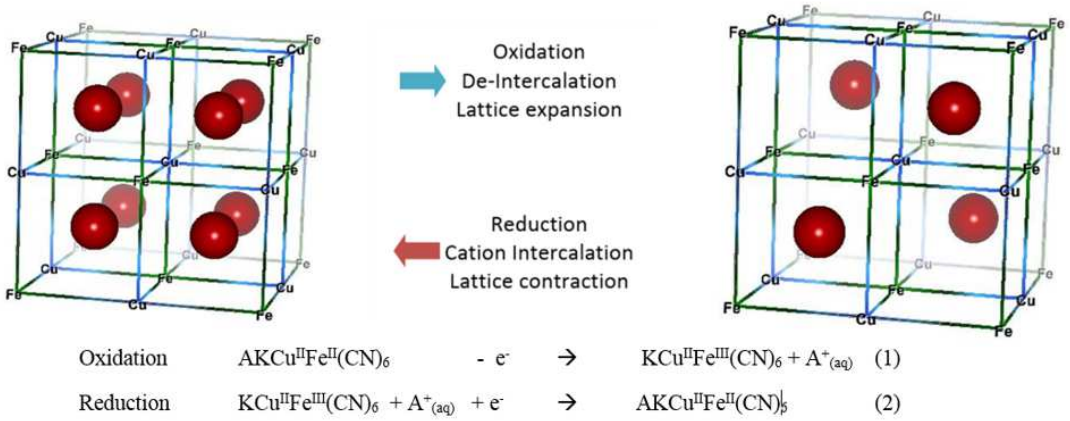

$$\text{Oxidation} \quad AKCu^{II}Fe^{II}(CN)_6 \; - e^- \rightarrow KCu^{II}Fe^{III}(CN)_6 + A^+_{(aq)} \quad (1)$$

$$\text{Reduction} \quad KCu^{II}Fe^{III}(CN)_6 + A^+_{(aq)} + e^- \rightarrow AKCu^{II}Fe^{II}(CN)_6 \quad (2)$$

Fig. 1 Crystal structure of $K_2CuFe(CN)_6$ in the discharged (intercalated) and the charged (de-intercalated) state. K^+ ions are shown in red and C≡N bonds are not shown for clarity. Fe and Cu lattice positions are labelled accordingly.

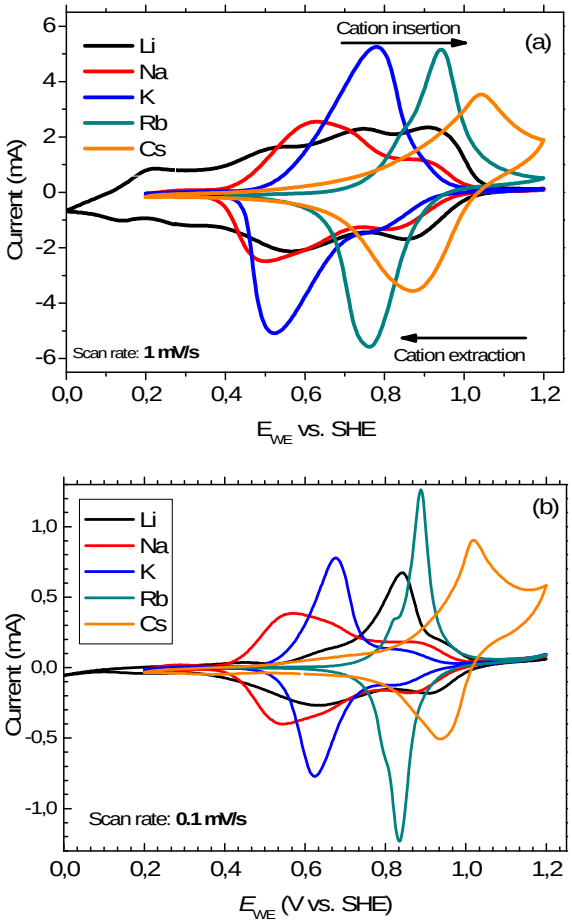

Fig. 2 Cyclic voltammetry at (a) 1 mV s^{-1} and (b) 0.1 mV s^{-1} on PBA under different itinerant cations.

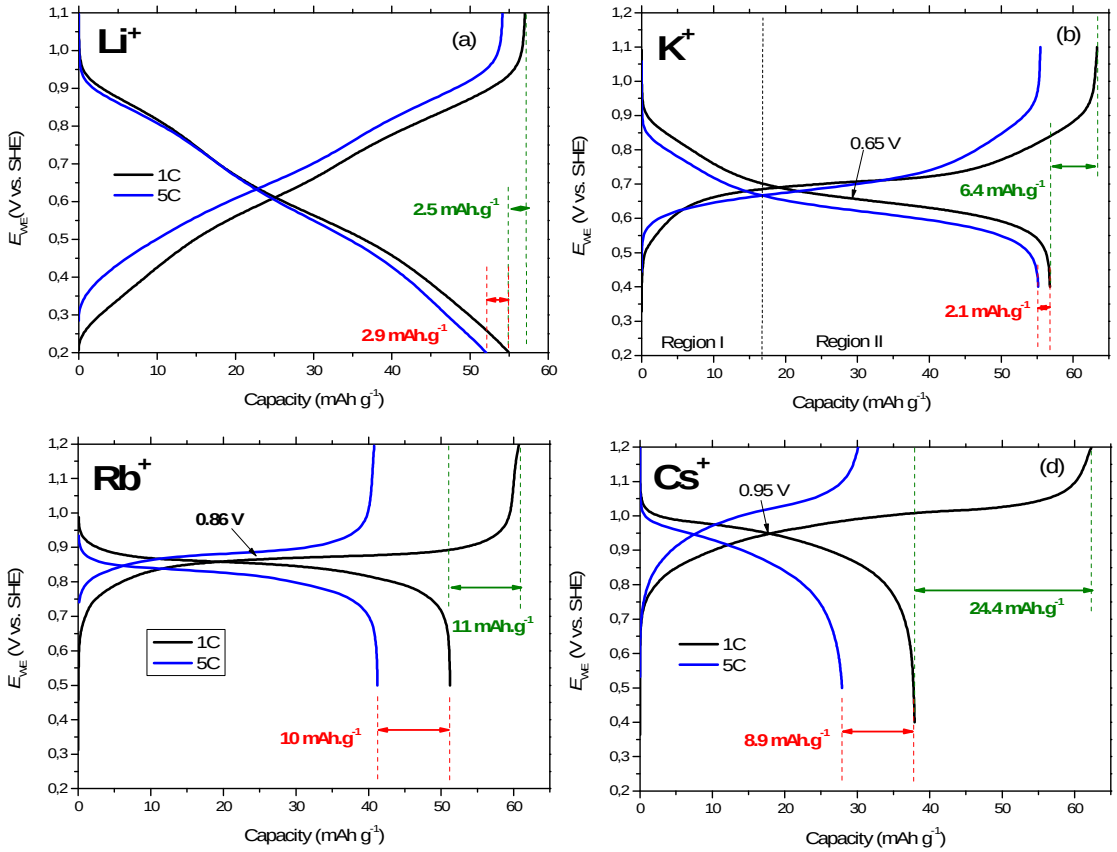

Fig. 3 Charge and discharge potential profile for the first cycle at 1C and 5C in electrolytes with different cations (a) Li^+, (b) K^+, (c) Rb^+ and (d) Cs^+. The reduction in discharge capacity (mAh g^{-1}) upon increasing the current from 1 C to 5 C is shown in red. The unrecoverable capacity of the first charge at 1 C is labelled in green.

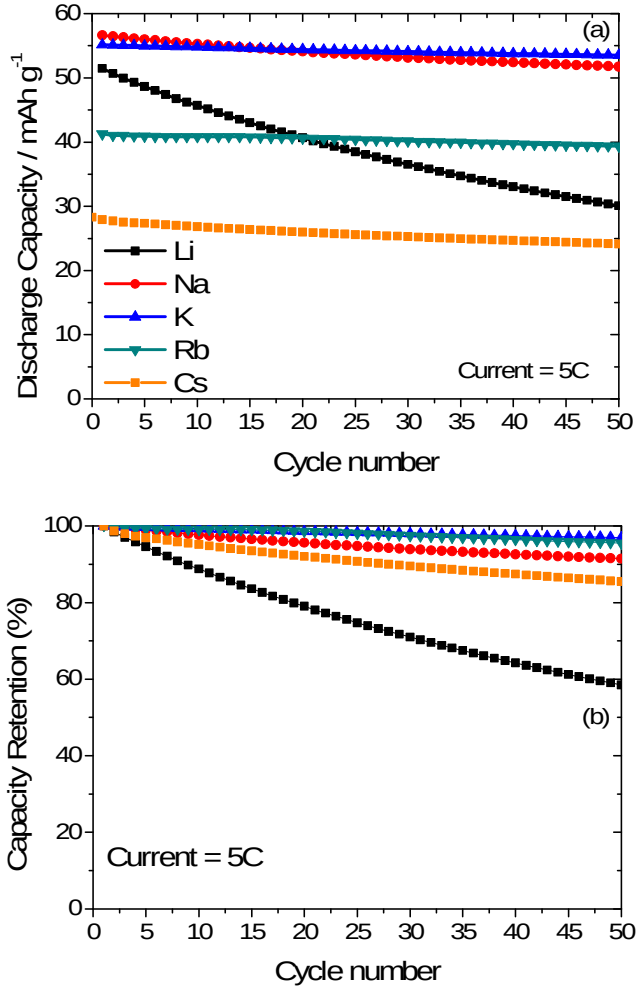

Fig. 4 Discharge capacity expressed in mAh g^{-1} (a) and normalized discharge capacity (b) as a function of the cycle number for PBA under galvanostatic cycling (5 C) with different itinerant cations.

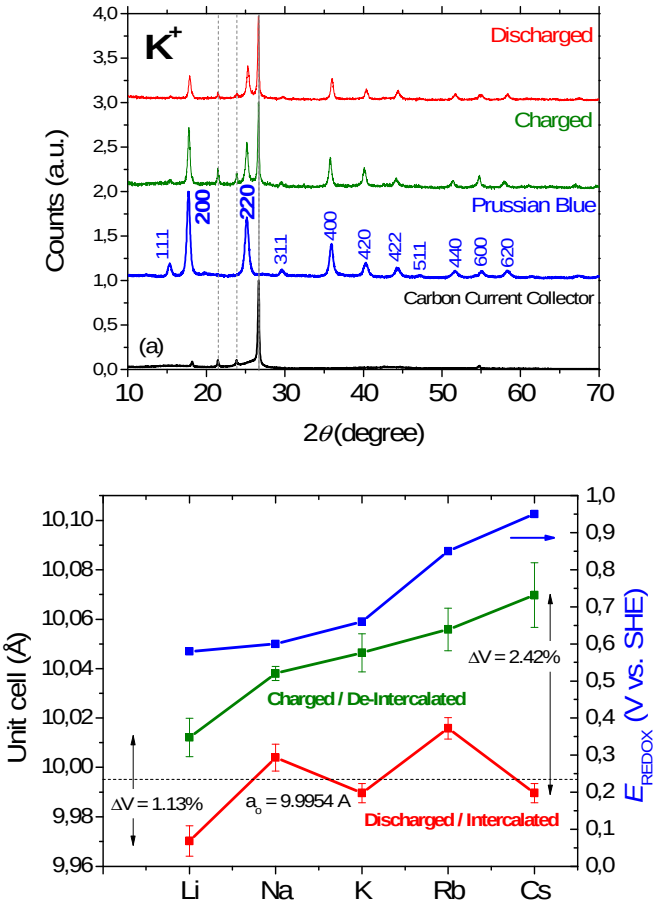

Fig. 5 (a) Obtained XRD patterns for pristine PBA (blue), PBA in the charged/de-intercalated state (green) and in the discharged/intercalated state (red). Pattern for uncoated carbon current collector also shown (black). (b) Calculated unit cell parameters from the XRD measurements as a function of the insertion cation for the PBA material in the intercalated state (red) and the de-intercalated state (green). Also shown are the respective measured redox potentials.

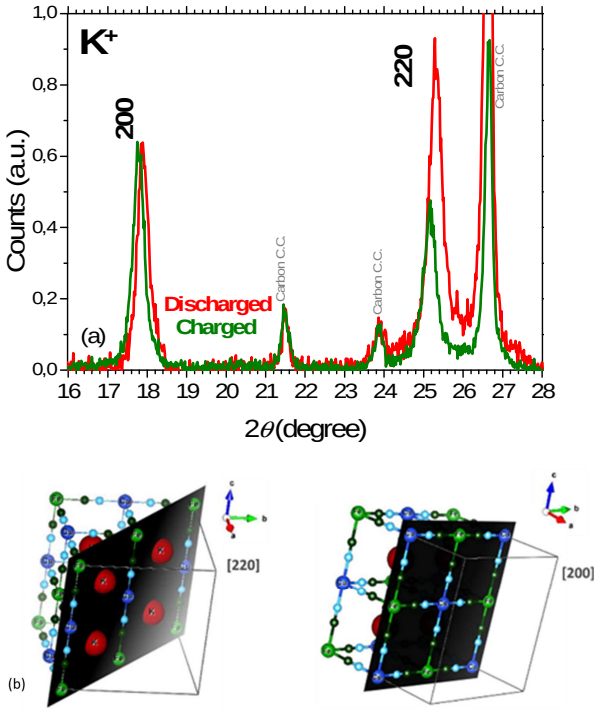

Fig. 6 (a) Superimposed XRD pattern of PBA in the intercalated (discharged) and de-intercalated (charged) state. Itinerant cation is K^+. (b) Crystallographic planes [220] and [200] corresponding to two prominent peaks observed in the powder XRD pattern.

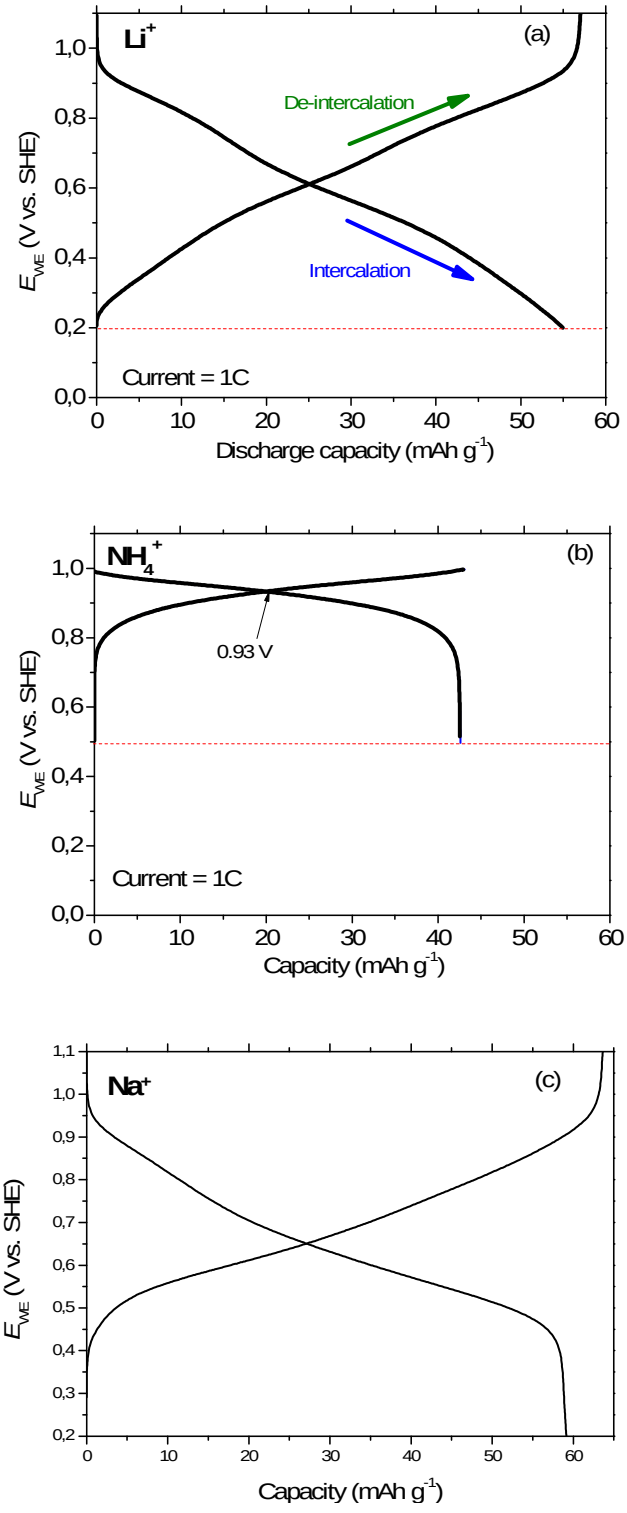

Fig. 7 Galvanostatic charge discharge curve for PBA with (a) Li^+, (b) NH_4^+ and (c) Na^+ itinerant cation at 1 C rate. Cations are inserted during discharge and vice versa as indicated.

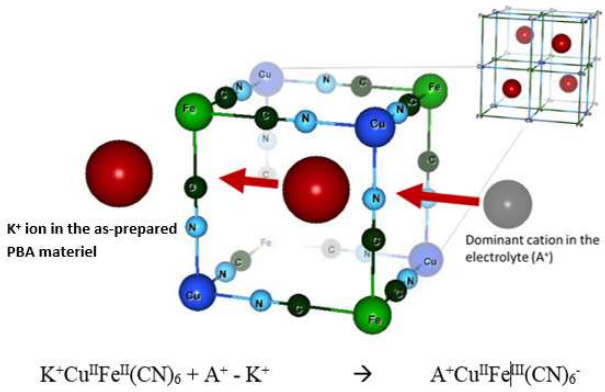

$$K^{+}Cu^{II}Fe^{II}(CN)_6 + A^{+} - K^{+} \rightarrow A^{+}Cu^{II}Fe^{III}(CN)_6^{-}$$

Fig. 8 Sub-section of the PBA unit cell showing the arrangement of Fe, Cu, C and N atoms around the itinerant cation. Dominant cation in the electrolyte (grey) depends on the electrolyte composition and could be Li^+, Na^+, K^+, Rb^+, Cs^+ which may be freely exchanged with the K^+ cation present in the as-synthesized material.

TOC

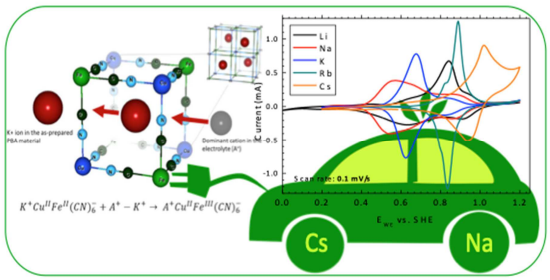

The redox behaviour of Prussian blue analogue (PBA) material was investigated with 5 aqueous alkali nitrate electrolytes (Li^+, Na^+, K^+, Rb^+, Cs^+) showing crystallographic plane variation of PBA depending on the state of charge.